Average angular momentum in compound nucleus reactions deduced from isomer ratio measurements

O. A. Capurro, D. E. DiGregorio, S. Gil, D. Abriola, M. di Tada, J. O. Fernández Niello, A. O. Macchiavelli,*
G. V. Martí, A. J. Pacheco, J. E. Testoni, D. Tomasi, and I. Urteaga
Laboratorio TANDAR, Departamento de Física, Comisión Nacional de Energía Atómica, Av. del Libertador 8250, 1429 Buenos Aires, Argentina
(Received 7 August 1996)

We have measured the ratio of the yields for the metastable and ground states of ^{119}Te produced in the fusion-evaporation reactions ^{110}Pd(^{12}C,3n) and ^{115}In(^{7}Li,3n) by off-line observation of delayed γ-ray emission. The absolute cross sections for the formation of the metastable ($J^{\pi} = 11/2^{-}$, $T_{1/2} = 4.68$ d) and ground ($J^{\pi} = 1/2^{+}$, $T_{1/2} = 16.05$ h) states were determined at energies close to the Coulomb barrier for both systems. We have deduced the average angular momentum from these isomer ratio measurements through statistical model calculations. The deduced mean angular momentum agrees quite well with those calculated by a simple fusion model. The expected constant value of the average total angular momentum at subbarrier energies was confirmed for the ^{12}C+^{110}Pd system. The predicted variation of the mean orbital angular momentum with the reduced mass of the entrance channel was also verified. [S0556-2813(97)04302-1]

PACS number(s): 25.70.Jj, 25.70.Gh

I. INTRODUCTION

The fusion cross sections can be described in terms of a partial wave expansion. The total fusion cross section is proportional to the zeroth moment of the compound nucleus spin distribution and the average angular momentum is its first moment. At energies near and above the Coulomb barrier, the average angular momentum decreases as the bombarding energy is lowered. Well below the Coulomb barrier, however, it is expected that the shape of angular momentum distribution leading to fusion does not change as a function of energy [1]. In particular, this prediction implies a saturation of the average angular momentum at sub-barrier energies. In this work, we have investigated these predictions through the study of the ^{12}C+^{110}Pd and ^{7}Li+^{115}In systems.

Various experimental techniques have been applied to the measurement of the first moment of the compound nucleus spin distribution: the γ-ray multiplicities (average [2–7] or distribution [8–12]), the population of levels belonging to the ground-state rotational band [13], the yields of evaporation residues produced after neutron emission [14,15] and the isomer ratios [16–18]. All these methods have been widely discussed and analyzed in recent articles ([19,20], and references therein).

Among these experimental probes, we have chosen the isomer-ratio technique which consists in measuring the ratio of the cross section for the population of a high spin isomeric state to that of a low spin ground state, to obtain the average angular momentum in the entrance channel. This method has been applied with great success for the isomeric pair in ^{137}Ce [16–18]. The ^{12}C+^{110}Pd and ^{7}Li+^{115}In systems lead to the compound nucleus ^{122}Te, which, after evaporating three neutrons and emitting γ rays, populates two isomeric states in ^{119}Te. A partial decay scheme for the isomeric ($J^{\pi} = 11/2^{-}$, $T_{1/2} = 4.68$ d) and ground ($J^{\pi} = 1/2^{+}$, $T_{1/2} = 16.05$ h) states in ^{119}Te is shown in Fig. 1. The measured 3n evaporation channel is the dominant decay mode for fusion of ^{12}C+^{110}Pd at bombarding energies close and below the Coulomb barrier, while for fusion of ^{7}Li+^{115}In the same channel is dominant at energies close and above the barrier. These systems have been studied at bombarding energies that produce the compound nucleus ^{122}Te at the same excitation energies.

The relationship between the measured isomer ratios and the average angular momenta in the compound nucleus was performed through a statistical model calculation. The influence of the most relevant input parameters used in the corresponding code on the relative populations of both isomeric states was analyzed.

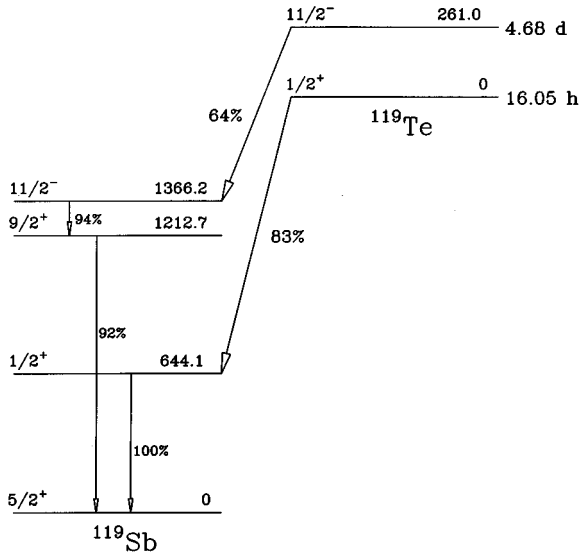

FIG. 1. A partial level scheme of ^{119}Te showing only the most intense decay paths of the metastable and ground states.

*Permanent address: Lawrence Berkeley Laboratory, Berkeley, California 94720.

 © 1997 The American Physical Society

The analysis of the data presented in this paper is an extension of a study of the experimental results published previously [21]. In Sec. II, the experimental procedure is briefly described and the results of the data analysis corresponding to both systems are reported. The comparison between our experimental results and model predictions is given in Sec. III. The theoretical models used in the calculations are described succinctly in the same section. In Sec. IV we discuss the relation between the isomer ratio and the average angular momentum and a method is proposed to deduce the latter from the former in $^{12}C+^{110}Pd$ and $^{7}Li+^{115}In$. This procedure is applied to obtain the first moment of the spin distribution in both systems. The deduced values of the average angular momentum are presented and compared with theoretical predictions in Sec. V. Finally, in Sec. VI we summarize this work and give our conclusions.

II. THE EXPERIMENT AND DATA ANALYSIS

The experiments were carried out with beams of ^{12}C and ^{7}Li ions provided by the 20-UD tandem accelerator at the TANDAR Laboratory in Buenos Aires. Beams of ^{12}C with laboratory energies from 36.5 to 54.0 MeV were used to bombard enriched palladium targets (96.98% ^{110}Pd, 2.35% ^{108}Pd). During the bombardments of ^{110}Pd targets, aluminium catcher foils with thicknesses of 0.65–0.95 mg/cm^2 were located behind the target to collect the evaporation residues. Bombarding energies of the ^{7}Li beams ranged from 20.4 to 37.1 MeV. Targets of ^{115}In were prepared by the evaporation of natural indium (95.7% ^{115}In, 4.3% ^{113}In) onto aluminium foils of 0.9 mg/cm^2 thickness. These aluminium backing foils act as catcher foils. In both cases, the target thicknesses varied between 150 μg/cm^2 and 250 μg/cm^2. Following bombardments the catcher foils were removed from the scattering chamber and placed in front of a high-purity germanium detector for off-line counting of the γ rays emitted by the different isotopes produced in the radioactive decay of the evaporation residues.

The γ-ray energy spectra were accumulated and recorded automatically at various time intervals during several hours. The energy resolution of the γ-ray detector was 2.0 keV [full width at half maximum (FWHM)] at 1332.5 keV and the total efficiency of the detector was $\sim$ 2% at 500 keV. During the bombardments, two silicon surface-barrier detectors were placed at $\pm$ 30° to the beam for monitoring the elastic scattering of the beam particles by the target nuclei. The profile of the beam current was recorded by multiscaling in 1-min intervals. The irradiation times varied between 2 and 10 h. Further details about this experimental procedure are described in a recent publication [21].

The presence of ^{119}Te was observed through the 1212.7 keV (I_γ = 66.7%) and 644.07 keV (I_γ = 84.5%) transitions corresponding to the decay of the metastable and ground states of the nucleus, respectively. The absolute γ-ray intensities were taken from Ref. [22]. Figure 2 shows a photon spectrum associated with the fusion reaction for $^{12}C+^{108,110}Pd$ at E_{lab} = 41.0 MeV. Figure 3 shows an off-line spectrum for $^{7}Li+^{113,115}In$ at a bombarding energy of E_{lab} = 27.5 MeV. The different γ-ray peaks come from the decay of evaporation and transfer residues.

The production rate of each isomeric state of ^{119}Te was determined from the peak area of the corresponding γ ray, its absolute intensity, the detector efficiency, and by extrapolating the decay curve at the end of the bombardment. Corrections were made to take into account the variation of the beam intensity during the bombardment and the finite length of the counting interval. Then, an absolute measurement for the production rate of each isomeric state of ^{119}Te was obtained by normalizing to Rutherford scattering. The isomer ratio was obtained dividing the absolute cross sections corresponding to the formation of the high spin isomeric state and the low spin ground state of ^{119}Te: $R=\sigma_{3n(\mathrm{m.s.})}/\sigma_{3n(\mathrm{g.s.})}$.

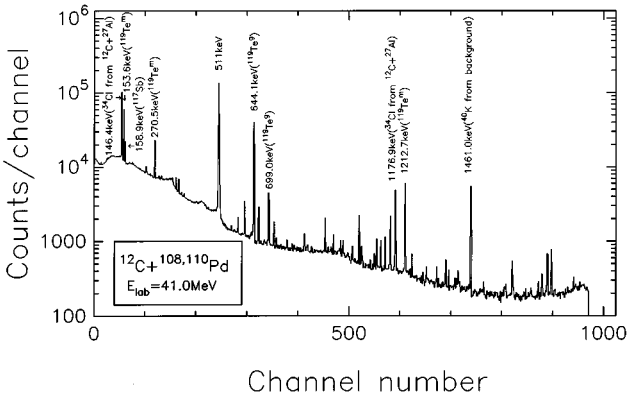

FIG. 2. Off-line energy spectrum obtained with a Ge detector for $^{12}C+^{108,110}Pd$ at laboratory bombarding energy of E_{lab}=41.0 MeV showing the delayed γ rays emitted from the radioactive residues.

The various sources of error on the cross sections corresponding to the formation of metastable and ground states were estimated as follows: absolute normalization based on Rutherford scattering, 6%; γ-ray detector efficiency, 4% for $^{12}C+^{110}Pd$ and 15% for $^{7}Li+^{115}In$; peak areas, $<$ 8% (except for $\sigma_{3n(\mathrm{m.s.})}$ in $^{12}C+^{110}Pd$ at the two lowest bombarding energies); and absolute γ-ray intensity, $<$ 1%. The uncertainty associated to the normalization is purely systematic. The uncertainty corresponding to the γ-ray detector efficiency is partly random and partly systematic. The uncertainties in the absolute normalization based on Rutherford scat-

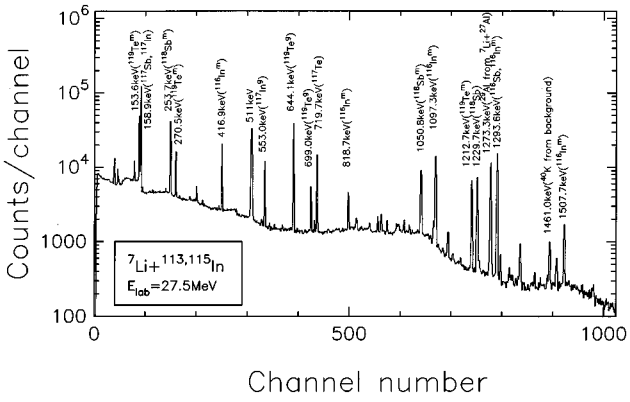

FIG. 3. Off-line energy spectrum obtained with a Ge detector for $^{7}Li+^{113,115}In$ at laboratory bombarding energy of E_{lab}=27.5 MeV showing the delayed γ rays emitted from the radioactive residues.

TABLE I. Experimental 3*n* evaporation channel cross sections and isomer ratios for $^{12}C+^{110}Pd$. Uncertainties only include statistical errors.

$E_{c.m.}$ (MeV)	^{119m}Te $\sigma_{3n(m.s.)}$ (mb)	^{119g}Te $\sigma_{3n(g.s.)}$ (mb)	Isomer ratio $\sigma_{3n(m.s.)}/\sigma_{3n(g.s.)}$
48.7	138.2 ± 1.2	17.89 ± 0.13	7.72 ± 0.09
46.0	164.3 ± 1.0	26.25 ± 0.10	6.26 ± 0.04
43.3	192.4 ± 1.5	43.49 ± 0.18	4.42 ± 0.04
41.5	158.9 ± 0.9	44.72 ± 0.12	3.55 ± 0.02
39.7	105.0 ± 1.3	40.94 ± 0.16	2.56 ± 0.03
37.9	65.1 ± 1.4	36.34 ± 0.17	1.79 ± 0.04
37.0	36.20 ± 0.58	20.12 ± 0.10	1.80 ± 0.03
36.1	21.06 ± 0.80	15.59 ± 0.10	1.35 ± 0.05
35.6			1.24 ± 0.07
35.2	7.21 ± 0.26	5.17 ± 0.03	1.39 ± 0.05
34.7	3.91 ± 0.13	3.13 ± 0.02	1.25 ± 0.04
34.3	1.85 ± 0.11	1.62 ± 0.02	1.14 ± 0.07
33.8	1.08 ± 0.15	1.06 ± 0.01	1.02 ± 0.14
33.4	0.54 ± 0.13	0.45 ± 0.01	1.20 ± 0.29
32.9		0.26 ± 0.02	

tering are cancelled when one calculates the isomer ratios. Tables and figures only include statistical errors unless otherwise indicated. The center-of-mass bombarding energies given in all tables correspond to the energy at the middle of the target. The beam energy was determined to an accuracy of 1%.

The absolute cross sections for the formation of the metastable and ground states of ^{119}Te for $^{12}C+^{110}Pd$ and $^{7}Li+^{115}In$ are reported in Tables I and II, respectively. These data are a complement of the experimental results reported elsewhere [21]. A new irradiation was performed for the $^{12}C+^{110}Pd$ system at the lowest energies to improve the statistics corresponding to the ^{119m}Te formation. The absolute cross sections for the formation of the metastable and

TABLE II. Experimental 3*n* evaporation channel cross sections and isomer ratios for $^{7}Li+^{115}In$. Uncertainties only include statistical errors.

$E_{c.m.}$ (MeV)	^{119m}Te $\sigma_{3n(m.s.)}$ (mb)	^{119g}Te $\sigma_{3n(g.s.)}$ (mb)	Isomer ratio $\sigma_{3n(m.s.)}/\sigma_{3n(g.s.)}$
35.0	184.7 ± 5.7	35.45 ± 0.62	5.21 ± 0.18
32.3	256.0 ± 6.3	55.17 ± 0.77	4.64 ± 0.13
29.6	369.3 ± 6.0	92.94 ± 0.76	3.97 ± 0.07
27.8	396.1 ± 9.4	132.10 ± 0.11	3.00 ± 0.07
26.0	381.5 ± 5.8	143.40 ± 0.78	2.66 ± 0.04
24.2	297.8 ± 5.8	144.5 ± 1.4	2.06 ± 0.04
22.4	187.9 ± 4.3	108.00 ± 0.68	1.74 ± 0.04
21.5	145.6 ± 3.6	87.16 ± 0.56	1.67 ± 0.04
20.6	92.7 ± 3.4	63.15 ± 0.50	1.47 ± 0.06
20.1	65.2 ± 2.8	47.19 ± 0.47	1.38 ± 0.06
19.7	37.4 ± 2.9	34.72 ± 0.45	1.08 ± 0.08
19.2	32.3 ± 1.9	23.72 ± 0.27	1.36 ± 0.08

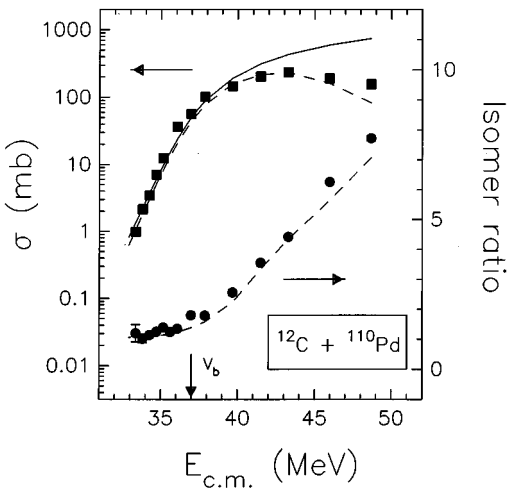

FIG. 4. Experimental 3*n* evaporation channel cross sections (left ordinate) and their associated isomer ratios (right ordinate) for $^{12}C+^{110}Pd$. The solid line is an estimate of the fusion cross section and the dashed curves are the predictions of statistical model. All these calculations are described in the text.

ground states of ^{119}Te for $^{12}C+^{110}Pd$ at $E_{c.m.}=35.6$ MeV cannot be obtained due to normalization problems. In addition, the poor statistics of the 1212.7 keV transition corresponding to ^{119m}Te for the same reaction at the lowest bombarding energy has not allowed us to get a reliable value of the associated cross section. Figures 4 and 5 show the experimental excitation functions for the 3*n* evaporation channel ($\sigma_{3n(m.s.)}+\sigma_{3n(g.s.)}$, full squares on the left axis) and the corresponding isomer ratios ($\sigma_{3n(m.s.)}/\sigma_{3n(g.s.)}$, full circles on the right axis) in both systems. As can be seen in these figures, the experimental isomer ratio decreases rapidly as the bombarding energy decreases down to the vicinity of the Coulomb barrier. In this energy region, there is a clear change in the slope for the $^{12}C+^{110}Pd$ system and the isomer

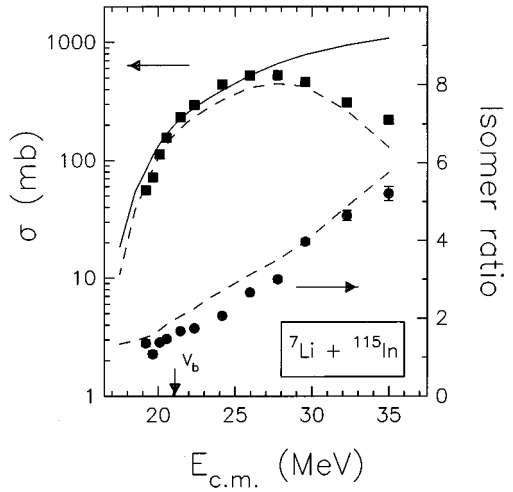

FIG. 5. Experimental 3*n* evaporation channel cross sections (left ordinate) and their associated isomer ratios (right ordinate) for $^{7}Li+^{115}In$. The solid line is an estimate of the fusion cross section and the dashed curves are the predictions of statistical model. All these calculations are described in the text.

ratio becomes essentially independent of energy (see Fig. 4). Although less pronounced, a gradual change in the slope is also observed for the ^{7}Li+ ^{115}In system (see Fig. 5).

III. COMPARISON WITH THEORETICAL MODELS

In order to compare the theory and the experiment, one must be able to obtain the fusion cross section and the spin distribution for the compound nucleus ^{122}Te from the 3n evaporation channel cross section and the isomer ratio for ^{119}Te. This is done by means of a statistical-decay model which, for a given excitation energy and angular momentum of the compound nucleus gives the probability of each evaporation channel and the relative population of the isomeric states. The fusion cross sections and the initial spin distributions in the compound nucleus needed as input in the statistical model calculations were obtained from a simple coupled-channel model for fusion.

A. Fusion model

The first step of the calculations was performed using a modified version of the code CCDEF [23] which follows the coupled-channel approach of Dasso and Landowne [1]. In this simplified coupled-channel model, the transmission coefficient for a partial wave l at the center-of-mass bombarding energy E is given by

$$T_l^{\mathrm{CCDEF}} = \sum_i \frac{p_i}{1+\exp\{[V_b + l(l+1)\hbar^2/2\mu R_b^2 + \lambda_i - E]/\epsilon\}}, \tag{3.1}$$

where ϵ is the curvature of the potential in the Hill-Wheeler approximation, p_i and λ_i are the relative flux and the barrier shift for the coupled channel i. The corresponding spin distribution $[\sigma_l = \pi/k^2(2l+1)T_l]$ follows different behavior above and below the Coulomb barrier. At energies above the barrier, σ_l has a triangular shape and the average angular momentum, $\langle l \rangle$, is given by

$$\langle l \rangle = \frac{2}{3}\sqrt{2\mu R_b^2 (E - V_b)/\hbar^2}. \tag{3.2}$$

At energies well below the Coulomb barrier, the shape of the l distribution turns bell-like and the corresponding $\langle l \rangle$ does not change with the energy:

$$\langle l \rangle = \frac{4}{3}\sqrt{\mu R_b^2 \epsilon/\hbar^2}. \tag{3.3}$$

The distributions of the compound-nucleus angular momentum were obtained including the coupling to the inelastic excitation of the target for the ^{12}C+ ^{110}Pd system and the coupling to the inelastic excitation of the target and to the transfer channels for the ^{7}Li+ ^{115}In system (see Ref. [21]).

B. Evaporation model

The statistical model calculations were done with the computer code PACE [24]. This Hauser-Feshbach compound nucleus decay code was chosen because it allows one to incorporate explicitly the low-lying levels of the residual nucleus, in particular the metastable and the ground states.

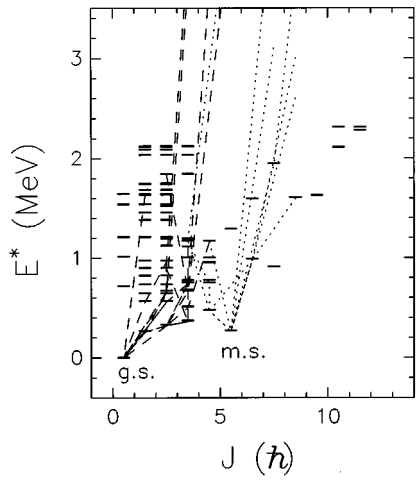

FIG. 6. Typical γ-ray deexcitation paths for some events of the 3n evaporation channel in the E^*-J plane. Generally, the evaporation residues with high (low) angular momentum will populate the isomeric state of highest (lowest) spin. The horizontal bars are the known high- and low-spin levels below 2.3 MeV excitation energy of ^{119}Te used to perform the statistical model calculations.

Thus, PACE performs a careful analysis of the last steps of the γ-ray deexcitation down to the metastable and ground states of the residual nucleus. Individual discrete states of ^{119}Te below 2.3 MeV excitation energy were included as input parameters of the code. This information was obtained from studies of the radioactive decay of ^{119}I and in the ^{117}Sn $(\alpha,2n)$, ^{120}Te(d,t), ^{120}Te$(^3$He,$\alpha)$ reactions [25]. Figure 6 shows the last steps of the γ-ray deexcitation for some events corresponding to the 3n evaporation channel in the excitation-energy–angular-momentum plane. The dotted lines indicate different events that finally populate the metastable state. While the dashed lines correspond to events whose disintegration paths finish in the ground state. The discrete levels below 2.3 MeV excitation energy (horizontal bar) are also shown in this figure. The level density formalism of Gilbert and Cameron [26] was employed above 2.3 MeV excitation energy with a level density parameter of $a = A/9.5$ MeV^{-1}. The reduced γ transitions of 0.000 1, 0.01, 9, and 1.2 Weisskopf units (W.u.) for the $E1$, $M1$, $E2$, and $M2$ transitions, respectively, were used in the description of the γ competition. The γ strengths and the level density parameter used in this work are sligthly different from those adopted in Ref. [21]. However, the relative xn yields are quite insensitive to these changes. Penetrabilities for particle emission were determined using the optical model potentials of Refs. [27,28].

As was remarked in Ref. [18], the moment of inertia which defines the yrast line is a very sensitive parameter that influences both the relative xn yields and the isomer ratios. Below 2.3 MeV excitation energy, the yrast line defined by the known states with the lowest excitation energy for each spin up to $J = 23/2\hbar$ was used to perform the statistical calculations. Due to the lack of discrete spectroscopy information above 2.3 MeV and for higher spins, we have used the rotational energies calculated by Gilbert and Cameron [26]. We found the experimental results (both the relative xn yields and the isomer ratios) to be in very good agreement with the model expectations. We also explored the conse-

quences on the population of the metastable and ground states by compelling the residual nucleus to follow a γ-ray deexcitation in accordance with the spectroscopic studies of ^{119}Te [25]. In other words, with the code PACE we followed each cascade down to the point where a known level of the residual nucleus is reached. Then, the following γ-ray deexcitation steps were carried out obeying the adopted γ-ray transition strenghs taken from Ref. [25]. Practically, no differences were found between this calculation and that performed completely by PACE.

C. Comparison with experiment

Figures 4 and 5 display the experimental 3*n* cross sections (left ordinate) and isomer ratios (right ordinate) compared with the predictions of the models described above. The solid curve is a calculation of the total fusion excitation function obtained with the simplified coupled-channel code CCDEF. The dashed curves represent the predicted 3*n* channel cross section (left ordinate) and isomer ratios (right ordinate) obtained by combining the above mentioned fusion model with the statistical model PACE. As can be seen, the result of the calculations for the isomer ratios is quite good all over the energy region for the ^{12}C+^{110}Pd system (Fig. 4). Furthermore, the agreement obtained is good even when the 3*n* channel is not the dominant decay mode for fusion evaporation. Instead, the predicted isomer ratios are slightly higher than our data for the ^{7}Li+^{115}In system (Fig. 5). It must be noted that the error bars of the experimental isomer ratios plotted in Figs. 4 and 5 only include pure statistical uncertainties. As was mentioned in Sec. II, the error on the γ-ray detector efficiency was 15% for the measurements in the ^{7}Li+^{115}In system. Therefore, the discrepancies observed between calculated and measured isomer ratios might be originated in this uncertainty. Nevertheless, the behavior of the experimental isomer ratio with the bombarding energy follows the expected variation according to CCDEF and PACE.

D. Evolution of the spin distribution with the energy

To illustrate the predicted evolution of the spin distributions (of the compound nucleus, 3*n* evaporation channel, and its two components: ground and metastable states) with the energy, we plotted them in Fig. 7 for the ^{12}C+^{110}Pd system at three bombarding energies. The angular momentum distributions of the compound nucleus were estimated by CCDEF for the coupling case (solid lines). With this l distribution (equal to J distribution since intrinsic spins of the reactants are zero for this system), the code PACE gives the relative yields corresponding to the 3*n* evaporation channel (dashed curves) and the formation of the metastable and ground states (dotted curves). The relative yields corresponding to $E_{\mathrm{c.m.}}$=41.5 MeV, 36.1 MeV, and 33.8 MeV are 69, 87, and 81% of the total fusion cross section, respectively. The initial spin distribution has approximately a triangular shape for the highest of these three energies. However, the shape becomes bell-like at subbarrier energies. In addition to this feature, the angular momentum distribution does not shift to lower J values, and therefore, the mean spin saturates below the Coulomb barrier. As can be seen in Fig. 7 at the two lowest energies, this is intimately related to the fact that the ratio between the yield of the metastable state and the ground state remains constant below a certain bombarding energy.

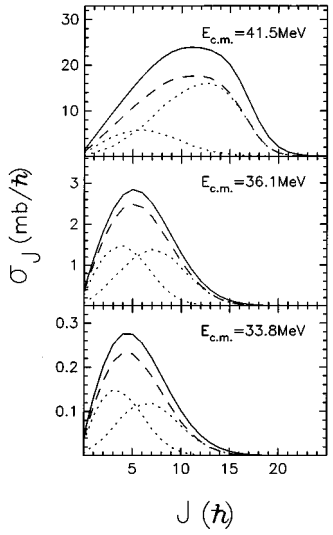

FIG. 7. Predicted angular momentum distributions at three bombarding energies for ^{12}C+^{110}Pd. The compound nucleus J distributions (solid lines) were estimated from a simplified coupled-channel calculations. Using these J distributions, a statistical model calculations give the 3*n* channel J distributions (dashed curves) and their two components metastable and ground states (dotted curves).

IV. AVERAGE ANGULAR MOMENTUM AND ISOMER RATIO

As was pointed out by DiGregorio *et al.* [18], it would be interesting to derive the average value of the initial spin distribution of the compound nucleus, a relevant characteristic quantity of the fusion-evaporation reaction, from measured isomer ratios without reference to a particular shape of the distribution. In this way a fusion model may be avoided, being only necessary to perform a statistical-decay model calculation. We will outline a procedure that allows such a derivation.

Denoting by s_1, s_2 the intrinsic spins of target and projectile and l the orbital angular momentum, the cross section for the formation of the compound nucleus with total angular momentum $\vec{J}=\vec{l}+\vec{S}$, being $\vec{S}=\vec{s_1}+\vec{s_2}$, can be written as

$$\sigma_J=\frac{\pi}{k^2}\frac{2J+1}{(2s_1+1)(2s_2+1)}\sum_{l=|J-S|}^{J+S}\sum_{S=|s_1-s_2|}^{s_1+s_2}T_{lSJ}\,, \tag{4.1}$$

where k is the wave number associated to the center-of-mass bombarding energy. We assume that the transmission coefficient, T_l, does not depend on S or J, and have a Fermi function shape,

$$T_l=\frac{1}{1+\exp[(l-l_0)/\Delta l]}\,. \tag{4.2}$$

We varied the parameters l_0 and Δl to obtain a wide family of distributions with different shapes that went from bell-like shapes for small l_0 and large Δl to triangular shapes for large l_0 and small Δl. The only constraint in these calculations

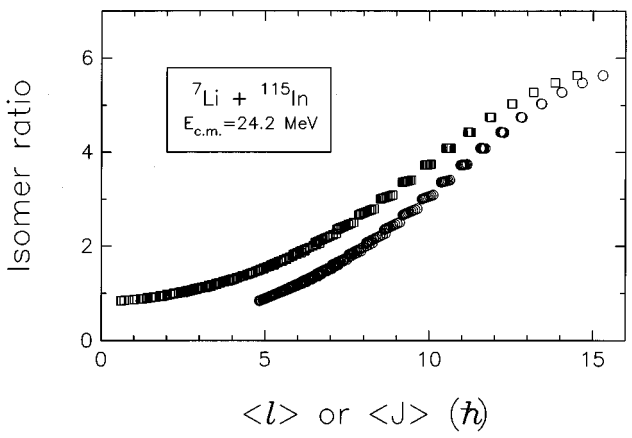

FIG. 8. Relation between the isomer ratio and the mean angular momentum for ^{7}Li+ ^{115}In (open squares for $\langle l \rangle$ and open circles for $\langle J \rangle$). This was performed through statistical model calculations using a Fermi function for the shape of the transmission coefficient. The family of these spin distributions goes from bell-like shape (small l_0 and large Δl) to triangular shape (large l_0 and small Δl).

was the highest partial wave $l_{\max}$. This $l_{\max}$ value is extracted from any appropriate fusion model. However, it can be remarked that an exact knowledge of the $l_{\max}$ value is not crucial for our calculations. The value of the mean angular momentum of the compound nucleus was evaluated as

$$\langle J \rangle = \frac{\Sigma_J J \sigma_J}{\Sigma_J \sigma_J} \tag{4.3}$$

and, in our case, the isomer ratio was calculated as

$$R = \frac{\sigma_{3n(\text{m.s.})}}{\sigma_{3n(\text{g.s.})}} = \frac{\Sigma_J Y_{J,3n(\text{m.s.})} \sigma_J}{\Sigma_J Y_{J,3n(\text{g.s.})} \sigma_J}, \tag{4.4}$$

where $Y_{J,3n(\text{m.s.})}$ ($Y_{J,3n(\text{g.s.})}$) is the relative yield of the metastable state (ground state) of ^{119}Te for the compound nucleus ^{122}Te at fixed excitation energy and total angular momentum. These relative yields are assumed to be valid for any entrance channel that leads to the same compound nucleus, that is, we have adopted the independence hypothesis for the decay of a compound nucleus. They are obtained through statistical model calculations with the input parameters described previously. The knowledge of these relative yields allow us to determine R for any initial spin distribution without an explicit statistical calculation for each one of them.

A. Correlation between $\langle J \rangle$ and R

Just to illustrate this method, Fig. 8 shows the results of the calculations corresponding to the ^{7}Li+ ^{115}In system (the ground state spins of these nuclei are $3/2\hbar$ and $9/2\hbar$, respectively) at $E_{\text{c.m.}}=24.2$ MeV. The wide family of spin distributions were obtained varying l_0 from $1\hbar$ to $22\hbar$ in steps of $0.5\hbar$, and Δl from $0.1\hbar$ to $3\hbar$ in steps of $0.1\hbar$. The correlation between $\langle l \rangle$ ($\langle J \rangle$) and R is shown in the figure with open squares (circles). The $l_{\max}$ value of $23\hbar$ was used as suggested by a CCDEF calculation. Because both $\langle l \rangle$ (or $\langle J \rangle$) and R are independent of $\sigma_{\text{fus}}=\Sigma_J \sigma_J$, we took the same arbitrary area for all the distributions. It must be noted that the intrinsic spins of both participant nuclei in this system are not equal to zero. At bombarding energies well above the Coulomb barrier, the effect of coupling the orbital angular momentum to the intrinsic spins of the reactants diminishes because of the high orbital angular momenta involved. Instead, the influence of this coupling is clearly important at near-barrier energies where the spin distributions are composed only by low orbital angular momenta. Although Fig. 8 corresponds to a single energy, the effect of such coupling can be inferred from the average angular momentum ($\langle l \rangle$ and $\langle J \rangle$) at high isomer ratios (high energies) and low isomer ratios (low energies). In summary, the correlation between the isomer ratio and the average angular momentum of the compound nucleus is almost single-valued. Therefore, one can deduce the mean value of the initial spin distribution measuring the isomer ratio of the dominant decay mode for fusion-evaporation even though the shape of the aforementioned distribution remains unknown.

B. Family of spin distributions for a given R

Now that a clear relation between the isomer ratio and the mean angular momentum of the compound nucleus has been demonstrated, we are ready to look at the quite restricted family of spin distributions that is compatible with a range of isomer-ratio values given by a certain R value and its corresponding error. Eight spin distributions of different shape were obtained from our calculations assuming $R=3.0\pm0.3$, and l_0 varying from $1\hbar$ to $22\hbar$ in steps of $1\hbar$ and Δl from $0.2\hbar$ to $3.0\hbar$ in steps of $0.2\hbar$. The isomer ratio value of 3.0 corresponds to the calculation performed with PACE for an initial spin distribution obtained from CCDEF($\langle l \rangle=8.4\hbar$ and $\langle J \rangle=9.7\hbar$). The percentual error in the isomer ratio was assumed to be 10%. The uncertainty in the deduced mean angular momentum will increase as the error in the isomer-ratio value is large. The value of the fusion cross section has no influence in the deduced average angular momentum as it has been pointed out in the previous paragraph. The eight spin distributions are plotted in Fig. 9(a) and their characteristic parameters reported in Table III. One can observe how l distributions of dissimilar shapes but comparable $\langle l \rangle$ ($\langle J \rangle$) lead to the same R. The effect of coupling the orbital angular momentum to the intrinsic spins of the reactants is illustrated in Fig. 9(b) where the observed differences in the shape of these eight l distributions are almost removed.

V. DEDUCED AND CALCULATED $\langle J \rangle$

We deduced the mean total angular momentum for both systems using the procedure described in the previous section. The total error in the isomer ratio was estimated summing in quadrature the statistical uncertainties and the corresponding error of the γ-ray detector efficiency. Therefore, the deduced $\langle J \rangle$ has an uncertainty coming from the total error in the experimental isomer ratio. The results are listed in Tables IV and V, and plotted in Figs. 10 and 11 (open circles, left ordinate). One can observe how the variations of the deduced $\langle J \rangle$ with the bombarding energy are accompa-

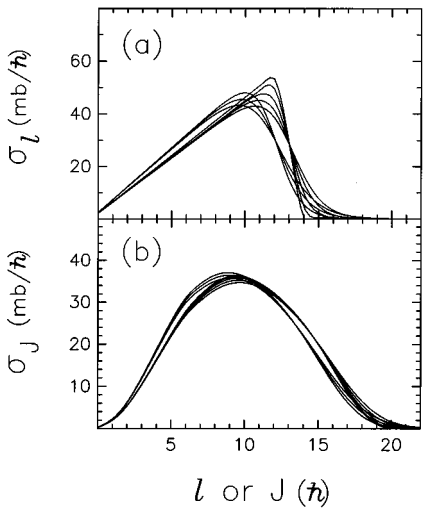

FIG. 9. (a) Family of l distributions corresponding to a ficticious value for the isomer ratio and its error. Several spin distributions of different shape were obtained varying l_0 and Δl at $E_{\text{c.m.}} = 24.2$ MeV (see the text for details of the calculations). (b) The consequence due to the coupling between the orbital angular momentum and the intrinsic spins of the reactants is illustrated.

nied by similar changes in the experimental R (solid circles, right ordinate) in both systems.

Our results were compared with fusion model calculations (CCDEF). The predictions are shown in Figs. 10 and 11. The solid curves are the result of simplified coupled-channel calculations with coupling to the inelastic excitation of target (in both systems) and to the transfer channels (in ^{7}Li $+ ^{115}$In). The dashed curves correspond to the isomer-ratio values obtained through statistical model calculations (PACE) using the spin distribution resulting from CCDEF for the coupling case. As can be seen in Fig. 10, the agreement achieved between the deduced and calculated mean angular momentum by CCDEF is quite good in the overall energy range for the ^{12}C$+ ^{110}$Pd system. Concerning the ^{7}Li$+ ^{115}$In system, the deduced values for the average total angular momentum are smaller than the fusion model predictions, as can be seen in Fig. 11. This is a natural consequence of our low experimental isomer ratios compared with the expectations in this system.

TABLE III. Different Fermi function spin distributions that produce almost the same average angular momentum for a given isomer ratio.

l_0 ($\hbar$)	Δl ($\hbar$)	$\langle l \rangle$ ($\hbar$)	$\langle J \rangle$ ($\hbar$)	R
12	0.8	8.1	9.4	2.72
12	1.0	8.2	9.5	2.75
12	1.2	8.3	9.6	2.79
13	0.2	8.5	9.8	3.00
13	0.4	8.6	9.8	3.01
13	0.6	8.6	9.9	3.03
13	0.8	8.7	10.0	3.05
13	1.0	8.8	10.1	3.07

TABLE IV. Deduced and calculated $\langle J \rangle$ for ^{12}C$+ ^{110}$Pd. Uncertainties in the values of $\langle J \rangle$ (deduced) come from statistical and systematic errors in the isomer ratios.

$E_{\text{c.m.}}$ (MeV)	$\langle J \rangle$ (deduced) ($\hbar$)	$\langle J \rangle_{\text{(CCDEF)}}$ ($\hbar$)	Difference (%)
48.7	17.6 ± 1.7	16.1	9.3
46.0	14.3 ± 0.5	14.2	0.7
43.3	11.8 ± 0.5	12.0	-1.7
41.5	10.8 ± 0.2	10.4	3.8
39.7	8.9 ± 0.3	8.9	0.0
37.9	7.5 ± 0.3	7.3	2.7
37.0	7.3 ± 0.2	6.6	10.1
36.1	6.3 ± 0.3	6.1	3.3
35.6	6.1 ± 0.3	5.9	3.4
35.2	6.4 ± 0.2	5.8	10.3
34.7	6.0 ± 0.2	5.7	-5.3
34.3	5.7 ± 0.3	5.7	0.0
33.8	5.4 ± 0.5	5.7	-5.3
33.4	5.7 ± 0.8	5.7	0.0

The highest yield of the $3n$ evaporation channel occurs near the Coulomb barrier for both systems. Therefore, one can get some relevant information about spin distributions at subbarrier energies where this channel is predominant over the others. Thus, the constancy of $\langle l \rangle$ ($\langle J \rangle$) at subbarrier energies predicted in Ref. [1] is verified unambiguously for ^{12}C$+ ^{110}$Pd by observing the deduced average total angular momentum in this energy region (see Fig. 10). For ^{7}Li $+ ^{115}$In the saturation of $\langle J \rangle$ has not been clearly reached at the lowest energies studied in this work (see Fig. 11). However, one can see that the deduced $\langle J \rangle$ values at these energies are similar when compared with the deduced limiting value in the other system. This is explained in terms of the coupling between the orbital angular momentum and the significant intrinsic spins of the projectile ^{7}Li ($3/2\hbar$) and the target ^{115}In ($9/2\hbar$). The consequence of such coupling is to shift the total spin distribution towards large J values. The

TABLE V. Deduced and calculated $\langle J \rangle$ for ^{7}Li$+ ^{115}$In. Uncertainties in the values of $\langle J \rangle$(deduced) come from statistical and systematic errors in the isomer ratios.

$E_{\text{c.m.}}$ (MeV)	$\langle J \rangle$ (deduced) ($\hbar$)	$\langle J \rangle_{\text{(CCDEF)}}$ ($\hbar$)	Difference (%)
35.0	12.9 ± 1.4	14.1	-8.5
32.3	11.9 ± 1.1	13.0	-8.5
29.6	11.3 ± 1.2	11.9	-5.0
27.8	9.7 ± 1.0	11.1	-12.6
26.0	9.2 ± 1.0	10.4	-11.5
24.2	8.1 ± 1.0	9.7	-19.8
22.4	7.3 ± 0.8	8.7	-16.1
21.5	7.1 ± 0.8	8.1	-12.3
20.6	6.6 ± 0.7	7.4	-10.8
20.1	6.4 ± 0.8	7.2	-11.1
19.7	5.5 ± 0.7	6.9	-20.3
19.2	6.3 ± 0.7	6.6	-4.5

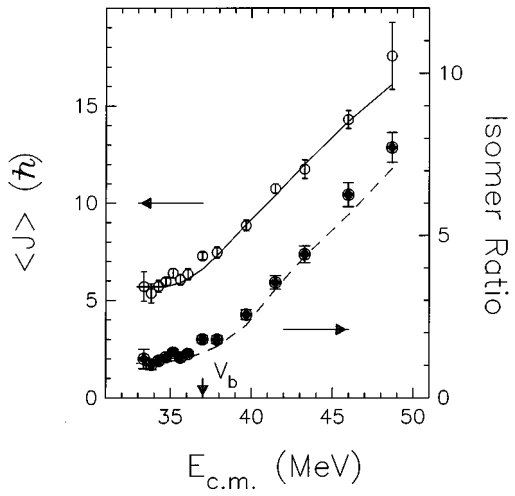

FIG. 10. Experimental isomer ratio (right ordinate) and deduced average angular momentum (left ordinate) for $^{12}C+^{110}Pd$. The total angular momentum is given by the orbital angular momentum because the intrinsic spins of the nuclei involved in this system are zero. The full line corresponds to the mean value of the l distributions estimated by CCDEF. The expected isomer ratio (dashed curve) is obtained from the evaporation code PACE employing such angular momentum distribution.

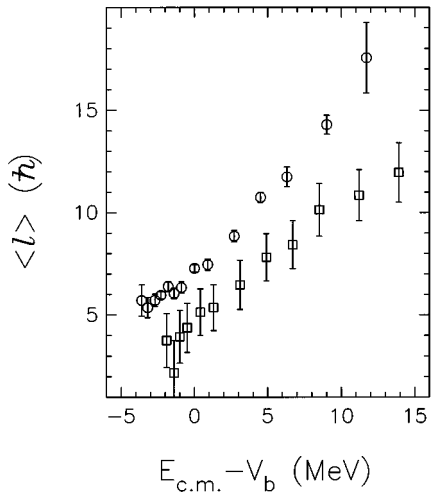

FIG. 12. The deduced average orbital angular momentum for both systems as a function of the difference between the center-of-mass bombarding energy and the Coulomb barrier energy. The open circles (squares) are the deduced $\langle l \rangle$ for $^{12}C+^{110}Pd$ ($^{7}Li+^{115}In$).

expected variation of $\langle l \rangle$ with the reduced mass of the entrance channel at energies well above and below the Coulomb barrier [Eqs. (3.2) and (3.3), respectively] was also tested for these systems. We show in Fig. 12 the corresponding deduced $\langle l \rangle$ as a function of $E_{c.m.}-V_b$. Our results ratify the predictions of simplified coupled-channel calculations about the behavior of the average orbital angular momentum with the reduced mass of the entrance channel at higher energies. The constancy of $\langle l \rangle$ for $^{7}Li+^{115}In$ at the lowest bombarding energies studied is not attained.

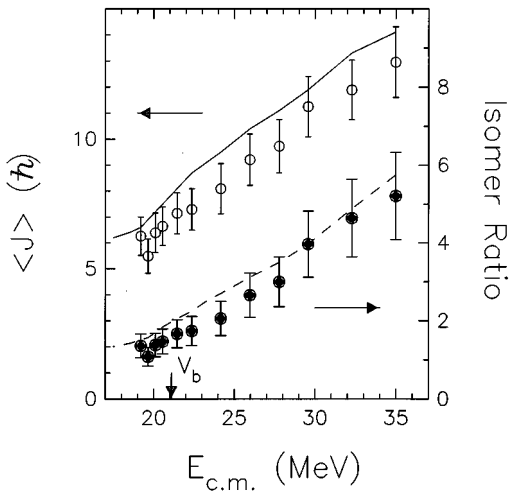

FIG. 11. Experimental isomer ratio (right ordinate) and deduced average angular momentum (left ordinate) for $^{7}Li+^{115}In$. The l distribution estimated by the code CCDEF is converted to a J distribution attending the intrinsic spins of the participant nuclei. The full line corresponds to the mean value of these calculated J distributions. The expected isomer ratio (dashed curve) is obtained from the evaporation code PACE employing such a total angular momentum distribution.

VI. SUMMARY AND CONCLUSIONS

In the present work, we have measured the populations of two isomeric states of ^{119}Te produced by fusion evaporation in the asymmetric systems $^{12}C+^{110}Pd$ and $^{7}Li+^{115}In$. The ratio between the yields for the metastable ($J^{\pi}=11/2^{-}$, $T_{1/2}=4.68$ d) and ground ($J^{\pi}=1/2^{+}$, $T_{1/2}=16.05$ h) states was obtained at sub- and near-barrier energies for the first system and at near- and above-barrier energies for the second system. The detection and identification of the corresponding evaporation residues was made through off-line observation of delayed γ-ray emission.

We have deduced average angular momenta of the compound nucleus from isomer ratio measurements with the aid of a statistical model calculations. The agreement achieved between the values of the deduced mean angular momentum and those calculated by a fusion model is quite good for $^{12}C+^{110}Pd$ and rather suitable for $^{7}Li+^{115}In$. The predicted saturation of total spin distribution at subbarrier energies is clearly corroborated for the former system. The expected variation of the average orbital angular momentum with the reduced mass of the entrance channel was also confirmed at energies above and below the Coulomb barrier.

To perform our calculations we have assumed the simple Fermi function for the shape of the transmission coefficient. Thus, one can obtain a family of spin distributions whose l_0 and Δl satisfies the constraints imposed by the σ_{fus} and l_{max} values. The spin distributions thus obtained are generally different to those estimated by CCDEF. However, the deduced mean angular momentum for both systems is almost independent of the spin distribution shape. The only requirement of this technique is to achieve a reasonable fit to the experimental isomer ratio.

Although this experimental method is limited in the number of systems which are practical for study, the present

work and that corresponding to the isomeric pair of ^{137}Ce [16,18] demonstrate clearly that the isomer ratio technique is a powerful means to determine the average angular momentum of the compound nucleus.

ACKNOWLEDGMENTS

Some of us (D.E.D.G., M.d.T., J.O.F.N., A.J.P., and J.E.T.) acknowledge the financial support of the Consejo Nacional de Investigaciones Científicas y Técnicas, Argentina.

[1] C. H. Dasso and S. Landowne, Phys. Rev. C **32**, 1094 (1985).
[2] R. Vandenbosch, B. B. Back, S. Gil, A. J. Lazzarini, and A. Ray, Phys. Rev. C **28**, 1161 (1983).
[3] S. Gil, R. Vandenbosch, A. J. Lazzarini, D. K. Lock, and A. Ray, Phys. Rev. C **31**, 1752 (1985).
[4] B. Haas, G. Duchene, F. A. Beck, T. Byrski, C. Gehringer, J. C. Merdinger, A. Nourredine, V. Rauch, J. P. Vivien, J. Barrete, S. Tobbeche, E. Bozek, J. Stycsen, J. Keinomen, J. Dudek, and W. Nazarewicz, Phys. Rev. Lett. **54**, 398 (1985).
[5] A. M. Stefanini, L. Corradi, D. Ackermann, A. Facco, F. Gramegna, H. Moreno, L. Meuller, D. R. Napoli, G. F. Prete, P. Spolaore, S. Beghini, D. Fabris, G. Montagnoli, G. Nebbia, J. A. Ruiz, G. F. Segato, C. Signorini, and G. Viesti, Nucl. Phys. **A548**, 453 (1992).
[6] D. Ackermann, L. Corradi, D. R. Napoli, C. M. Petrache, P. Spolaore, A. M. Stefanini, F. Scarlassara, S. Beghini, G. Montagnoli, G. F. Segato, and C. Signorini, Nucl. Phys. **A575**, 374 (1994).
[7] A. W. Charlop, J. D. Bierman, Z. Drebi, S. Gil, D. J. Prindle, A. Sonzogni, R. Vandenbosch, and D. Ye, Phys. Rev. C **51**, 628 (1995).
[8] P. J. Nolan, D. J. G. Love, A. Kirwan, D. J. Unwin, A. H. Nelson, P. J. Twin, and J. D. Garret, Phys. Rev. Lett. **54**, 2211 (1985).
[9] R. D. Fischer, A. Ruckelshausen, G. Koch, W. Kuhn, V. Metag, R. Muhlhans, R. Novotny, H. Stroher, H. Groger, D. Habs, H. W. Heyng, R. Repnow, D. Schwalm, W. Reisdorf, and R. S. Simon, Phys. Lett. B **171**, 33 (1986).
[10] M. L. Halbert, J. R. Beene, D. C. Hensley, K. Honkanen, T. M. Semkow, V. Abenante, D. G. Sarantities, and Z. Li, Phys. Rev. C **40**, 2558 (1989).
[11] G. Duchene, P. Romain, S. K. Basu, F. A. Beck, Ph. Benet, E. Bozek, D. E. DiGregorio, D. Disdier, J. O. Fernández Niello, B. Haas, B. Lott, V. Rauch, F. Scheibling, J. P. Vivien, and K. Zuber, Phys. Rev. C **47**, 2043 (1993).
[12] A. H. Wuosmaa, R. R. Betts, B. B. Back, M. P. Carpenter, H. Esbensen, P. B. Fernandez, B. G. Glagola, Th. Happ, R. V. F. Janssens, T. L. Khoo, E. F. Moore, F. Scarlassara, and Ph. Benet, Phys. Lett. B **263**, 23 (1991).
[13] J. D. Bierman, A. W. Charlop, D. J. Prindle, R. Vandenbosch, and D. Ye, Phys. Rev. C **48**, 319 (1993).
[14] M. Dasgupta, A. Navin, Y. K. Agarwal, C. V. K. Baba, H. C. Jain, M. L. Jhingan, and A. Roy, Phys. Rev. Lett. **66**, 1414 (1991).
[15] M. Dasgupta, A. Navin, Y. K. Agarwal, C. V. K. Baba, H. C. Jain, M. L. Jhingan, and A. Roy, Nucl. Phys. **A539**, 351 (1992).
[16] R. G. Stokstad, D. E. DiGregorio, K. T. Lesko, B. A. Harmon, E. B. Norman, J. Pouliot, and Y. D. Chan, Phys. Rev. Lett. **62**, 399 (1989).
[17] D. E. DiGregorio, K. T. Lesko, B. A. Harmon, E. B. Norman, J. Pouliot, B. Sur, Y. D. Chan, and R. G. Stokstad, *Proceedings of the XII Workshop on Nuclear Physics, Iguazú Falls, Argentina, 1989*, edited by M. C. Cambiaggio, A. J. Kreiner, and E. Ventura (World Scientific, Singapore, 1990), p. 44.
[18] D. E. DiGregorio, K. T. Lesko, B. A. Harmon, E. B. Norman, J. Pouliot, B. Sur, Y. Chan, and R. G. Stokstad, Phys. Rev. C **42**, 2108 (1990).
[19] D. E. DiGregorio and R. G. Stokstad, Phys. Rev. C **43**, 265 (1991).
[20] R. Vandenbosch, Annu. Rev. Nucl. Part. Sci. **42**, 447 (1992).
[21] O. A. Capurro, D. E. DiGregorio, S. Gil, D. Abriola, M. di Tada, J. O. Fernández Niello, A. O. Macchiavelli, G. V. Martí, A. J. Pacheco, J. E. Testoni, D. Tomasi, and I. Urteaga, Phys. Rev. C **53**, 1301 (1996).
[22] E. Browne and R. B. Firestone, *Table of Radioactive Isotopes* (Wiley Interscience, New York, 1986).
[23] J. O. Fernández Niello, C. H. Dasso, and S. Landowne, Comput. Phys. Commun. **54**, 409 (1989).
[24] A. Gavron, Phys. Rev. C **21**, 230 (1980).
[25] K. Kitao, M. Kambe, and K. Ogawa, Nucl. Data Sheets **67**, 327 (1992).
[26] A. Gilbert and A. G. W. Cameron, Can. J. Phys. **43**, 1446 (1965).
[27] C. M. Perey and F. G. Perey, At. Data Nucl. Data Tables **17**, 1 (1976).
[28] J. R. Huizenga and G. Igo, Nucl. Phys. **29**, 462 (1962).